

# Development of a Novel Simulator for Modelling Underground Hydrogen and Gas Mixture Storage

Zuansi Cai<sup>1,\*</sup>, Keni Zhang<sup>2,\*</sup>, Chaobin Guo<sup>3</sup>

<sup>1</sup>School of Engineering and the Built Environment, Edinburgh Napier University, Edinburgh EH10 5DT, UK

<sup>2</sup>Jinan University, China

<sup>3</sup>Chinese Academy of Geological Sciences, Beijing 100037, China

## Abstract

Underground hydrogen storage can store grid-scale energy for balancing both short-term and long-term inter-seasonal supply and demand. However, there is no numerical simulator which is dedicated to the design and optimisation of such energy storage technology at grid scale. This study develops novel simulation capabilities for GPSFLOW (**G**eneral **P**urpose **S**ubsurface **F**low Simulator) for modelling grid-scale hydrogen and gas mixture (e.g., H<sub>2</sub>-CO<sub>2</sub>-CH<sub>4</sub>-N<sub>2</sub>) storage in cavern, deep saline aquifers and depleted gas fields.

The accuracy of GPSFLOW is verified by comparisons against the National Institute of Standard and Technology (NIST) online thermophysical database and reported lab experiments, over a range of temperatures from 20-200 °C and pressure up to 1000 bar. The simulator is benchmarked against an existing model for modelling pure H<sub>2</sub> storage in a synthetic aquifer. Several underground hydrogen storage scenarios including H<sub>2</sub> storage in a synthetic salt cavern, H<sub>2</sub> injection into a CH<sub>4</sub>-saturated aquifer experiment, and hydrogen storage in a depleted gas field using CO<sub>2</sub> as a cushion gas are used to test the GPSFLOW's modelling capability. The results show that GPSFLOW offers a robust numerical tool to model underground hydrogen storage and gas mixture at grid scale on multiple parallel computing platforms.

**Keywords:** GPSFLOW, Underground H<sub>2</sub> and gas mixture storage, H<sub>2</sub> Thermodynamic model, Numerical simulation

\* Corresponding authors: E-mail address: z.cai@napier.ac.uk (Z. Cai); keniz@hotmail.com (K. Zhang)

## Introduction

To limit the rise in global temperature to 1.5 °C, a number of countries have pledged to reach net-zero greenhouse gas emissions by mid-century. The IEA's recent analysis suggests that in the net zero emissions scenario hydrogen will account for 13% (~ 510 million tonnes of H<sub>2</sub>) of global energy final demand in 2050, with 60% of hydrogen production coming from water electrolysis and the rest from natural gas in combination with carbon capture, utilization and storage [1]. The UK is the first major economy to set legally binding targets for achieving net-zero emissions by 2050. Hydrogen is identified to play a key role in achieving the UK's net-zero goal, primarily aiding the decarbonization of heating and long-distance travel such as heavy goods vehicles and ships [2].

It is estimated that by 2050 the UK will need 200-300 TWh of hydrogen use to meet the net zero target, with a storage capacity of at least 15 TWh (~450k tonnes of H<sub>2</sub>) storage capability to meet short-term and seasonal supply and demand variability [2-4]. Globally, although the total hydrogen storage capacity required to meet net zero emissions has not been reported in the IEA's recent analysis, it is, however, generally agreed that stored hydrogen can help balance both seasonal fluctuations in electricity demand and imbalance between hydrogen demand and its supply by renewable systems (e.g., [1, 4, 5]).

There are several different grid-scale hydrogen storage technologies including underground (e.g., depleted gas fields, aquifers, salt caverns, etc.) and above-ground storage facilities (e.g., pipeline and vessels). Each has its own advantages and constraints. Studies suggest that for seasonal large-scale storage, underground salt caverns and depleted gas fields are more favourable than above-ground storage technologies [4-6]. Although underground hydrogen storage is not a new concept, only three sites in the world currently store hydrogen in salt caverns in the UK and United States [7].

The increased use of hydrogen to meet net zero emissions will inevitably lead to an increased demand for hydrogen storage capacity. The limited geographical variability of salt formation is the main constraint for salt caverns being widely used for hydrogen storage. Therefore, the repurposing of existing underground gas storage facilities for grid-scale hydrogen storage would provide an attractive alternative. Globally, 680 underground gas storage facilities were in operation at the end of 2015. This represents a working natural gas capacity of 413 billion cubic metres, with 80% storage capacity in depleted gas/oil fields [7]. Being already established technologies for natural gas storage, none of these underground storage facilities have yet to be repurposed for hydrogen storage.

The knowledge gained by underground natural gas storage seems to be easily transferred to the case of hydrogen storage given the similarities in design, construction and operation. However, challenges remain for repurposing the existing gas facilities for hydrogen storage. Being the smallest chemical particle known, hydrogen gas has a high penetrability. It is more than 10 times lighter than methane in storage facilities, and migrates and diffuses in solids several times faster [8]. This requires the reassessment of caprock sealing capacity which is sufficient for natural gas. In addition, as natural gas is not easily dispersed as hydrogen gas, trap formation must be reviewed to ensure that steep anticline structures prevent lateral dispersion. Furthermore, injection of hydrogen gas into existing underground gas storage facilities is a multiphase and multi-component flow problem. The complex interactions of injected hydrogen gas with indigenous gases, minerals, dissolved solutes, microbial metabolisms and host rock must be assessed before field implementation.

For other underground hydrogen storage technologies, there is active research to explore the use of salt caverns for storing hydrogen and natural gas mixtures [9-11], which are produced using biomass or coal gasification. For saline aquifers, given that the cushion gas can take up to 80% of the

volumetric capacity of the storage [4, 12-14], to reduce the upfront investment required, nitrogen has been suggested to be used as the cushion gas [14, 15]. In our opinion, CO<sub>2</sub> would serve this purpose better. All the aforementioned underground storage technologies including hydrogen and natural gas mixture storage in salt caverns, the use of N<sub>2</sub> or CO<sub>2</sub> as the cushion gas to store hydrogen in saline aquifers or hydrogen storage in depleted gas fields are involved in multiphase and multi-component flow phenomena. To assess, design and optimise these technologies, a numerical tool capable of accounting for these processes is required.

Currently, there is no existing model which has been designed for modelling underground hydrogen and gas mixture storage, and can account for thermal, multiphase and multi-component flow. There are several numerical models including DuMU<sup>x</sup>, ECLIPSE, TOUGH, OpenGeoSys-ECIPSE and COMSOL [14-18]. Wallace et al. [4] conducted a comprehensive review of the application of these models for hydrogen storage, along with the advantages and constraints of each model. Overall, these simulators have been developed for other applications. None of them have been verified for underground hydrogen storage simulation, including the solubility of hydrogen and gas mixtures in water/saline solutions and thermodynamic models for estimating key flow parameters such as the density and viscosity of hydrogen and gas mixtures. For example, the study of hydrogen in porous rocks the ECLIPSE compositional model shows poor performance in history matching for hydrogen storage in a depleted gas reservoir [19]. Lysy et al. [20] used the solvent option of the ECLIPSE black oil model to simulate hydrogen flow processes. TOUGH+RealGas [21] provides simulation capability for subsurface flow processes with a mixture of gases including hydrogen. However, there are no reports regarding its application in hydrogen storage and no verification either.

The key objective of this research is to develop a novel and robust simulator, which is designed to model underground hydrogen and gas mixture storage at grid scale. The novel simulator considers non-isothermal, multiphase-multi-component flow within a heterogeneous reservoir, by solving equations of heat, multiphase (gas and aqueous) and multi-component (e.g., H<sub>2</sub>-CO<sub>2</sub>-CH<sub>4</sub>-N<sub>2</sub>) flow over a range of temperatures from 25-200 °C and pressure up to 1000 bar. With the application of several state-of-the-art parallel computing techniques, the simulator is capable of modelling hydrogen storage at grid scale on a multi-core PC, workstation, and high-performance computing facility.

The numerical simulator development in this study includes: 1) the deployment of a novel non-iterative fugacity-activity thermodynamic approach to calculate the solubility of the pure gas (e.g., H<sub>2</sub>, CO<sub>2</sub>, CH<sub>4</sub> and N<sub>2</sub>) and gas mixtures (e.g., H<sub>2</sub>-CO<sub>2</sub>-CH<sub>4</sub>-N<sub>2</sub>) in water and verification of the approach with available laboratory-reported data; 2) The development of a thermodynamic model for estimating density, viscosity and enthalpy of the pure gas and gas mixture based on the real gas law. The thermodynamic model was calibrated and/or verified by comparisons against the national institute of standards and technology (NIST) online thermophysical database; 3) The simulator was tested/benchmarked on five case studies including hydrogen storage in an aquifer, a salt cavern, a CH<sub>4</sub>-saturated aquifer experiment and in a depleted gas field as well as application of CO<sub>2</sub> as a cushion gas for hydrogen storage in a depleted gas field. With the efficient parallel computing schemes, these new developments will pave the way for extending GPSFLOW modelling capability to include chemical and mechanical processes. This could provide a foundation to assess the impacts of the biogeochemical reactions on the hydrogen loss in the storage facility, as well as impacts of the thermo-mechanical behaviour on caprock sealing capacity.

## Methodology

### Governing equations

GPSFLOW is a general purpose subsurface flow simulator developed in C++ Programming by [22]. It solves the governing equations for non-isothermal, multiphase, multi-component flows in porous or fractured media, which are similar to reservoir simulators such as TOUGH, ECLIPSE, OpenGeoSys and DuMU<sup>x</sup> [16, 17, 23]. This study extends the simulator for modelling gas mixtures for underground hydrogen storage. The governing equations are summarized in Table 1. For mass balance, the total sum of mass fraction ( $X_{\beta}^i$ ) in phase  $\beta$  must equal to 1. Capillary pressure ( $P_{c\beta}$ ) and relative permeability ( $k_{r\beta}$ ) equations are required to complete the solution of the resulting system of equations. GPSFLOW provides options to select different relative permeability and capillary pressure equations, including the Brooks-Corey model, van Genuchten model, etc. Sink and source terms are specified by the mass production ( $q < 0$ ) or injection ( $q > 0$ ) rates of fluids or operation pressure as well as heat flow. Sinks and sources can be either constant or time dependent. The wells are implemented either as sources/sinks or by using the virtual node approach [24].

### Mutual solubility of H<sub>2</sub>-CH<sub>4</sub>-CO<sub>2</sub>-N<sub>2</sub> gas mixture in water

A non-iterative activity-fugacity thermodynamic model was implemented in GPSFLOW to consider the mutual solubility of H<sub>2</sub>-CH<sub>4</sub>-CO<sub>2</sub>-N<sub>2</sub> gas mixtures in water. This model is based on local thermodynamic equilibrium. This means that there is equality of the chemical potential of each component in gas and liquid phases at equilibrium, which can be written as:

$$K_i = \frac{y_i}{x_i} = \frac{a_i}{f_i} \quad i = H_2, CH_4, CO_2 \text{ or } N_2 \quad (1)$$

where  $K_i$  is the equilibrium constant of component  $i$ ;  $y_i$  and  $x_i$  are mole fractions of component  $i$  in gas and liquid phases, respectively;  $a_i$  is the activity of component  $i$  in the aqueous phase and  $f_i$  is the fugacity of component  $i$  in the gas phase. Making use of  $a_i \approx \gamma_i 55.508 x_i$  and assuming 55.508 moles H<sub>2</sub>O per kg of aqueous phase and  $f_i = P \Phi_i y_i$ , Eq. (1) leads to:

$$K_i = \frac{y_i}{x_i} = \frac{55.508 \gamma_i}{P \Phi_i} \quad i = H_2, CH_4, CO_2 \text{ or } N_2 \quad (2)$$

where  $\gamma_i$  is the activity coefficient of component  $i$ ;  $P$  is the total pressure of gas phase and  $\Phi_i$  is the fugacity of component  $i$  in the gas phase.

To obtain the solubility of gases or mole fractions in both aqueous and gaseous phases, one of the mole fractions of each gas in either the aqueous or gaseous phase must be known, which can be treated as primary variables and solved directly from the mass balance equations. Gas mole fraction of a gas component is defined as the ratio of the amount of gas (expressed in moles) to the total amount of all gas components in a mixture (expressed in moles) including water vapour. For a two-phase flow system with  $ng$  gas components, the maximum number of mole fractions solved from the mass balance equation is  $ng-1$ . For example, for a two-phase (gas and liquid) flow with the components H<sub>2</sub>, CH<sub>4</sub>, CO<sub>2</sub>, N<sub>2</sub> and water ( $NK = 5$ ), the number of phases ( $NPH$ ) is 2 and  $ng$  is 4. In this case, the total number of variables which can be solved directly from the mass balance equations for each grid block is 5 (the same as  $NK$ ). These include pressure, phase saturation, and gas mole fractions of H<sub>2</sub>, CH<sub>4</sub> and CO<sub>2</sub>. Therefore, gas mole fractions of N<sub>2</sub> and water vapour remain unknown, while for single phase (gas or liquid) flow with the above four gas components, the gas mole fractions of H<sub>2</sub>, CH<sub>4</sub>, CO<sub>2</sub> and N<sub>2</sub> and pressure can be solved directly from mass balance equations as the phase saturation is known. Vapour mole fraction is then calculated by 1.0 minus the sum of the  $ng$  gas mole fractions.

For two-phase flow, TOUGH2/EOS7C [25] uses an iterative approach to solve the mole fractions of the last gas component and water vapour. This approach often suffers convergence problems in applications. To avoid the iteration process, a simple approach involves ignoring the water vapour in gas flow (such as TOUGH3/EOC7CA, [26]). However, vapour is a very important component in many applications, and it should be considered in the simulations. In this study, we used the normalised mole fraction defined by the ratio of the amount of a gas component in moles to total amount of all gas components in moles except water vapour. By this approach, the mole fraction of the last gas component in two-phase flow can be simply calculated by 1.0 minus the sum of the  $ng-1$  gas mole fractions which can be solved directly from the mass balance equations. Vapour mole fraction is then calculated as a function of the vapour partial pressure and temperature. Therefore, the mole fraction of each gas component in the gas phase can be corrected by calculating the ratio of the normalised mole fraction of the gas component to 1.0 plus vapour mole fraction. This gas-liquid equilibrium-based approach avoids the unstable iteration processes and a similar approach has been also used in an improved TOUGH2 module [27]. Given that vapour mole fraction in the gas phase is typically less than a few percentage points in most applications, the approach can provide an adequate accuracy.

Fugacity coefficients are calculated using the SRK EOS [28] cubic equation, combined with standard simple mixing rules and binary interaction coefficients. The binary interaction coefficients among  $H_2$ ,  $CH_4$ ,  $CO_2$ ,  $N_2$  and water vapour were obtained from published data [29-32]. Activities of  $H_2$ ,  $CH_4$  and  $N_2$  were calculated using the salting out coefficients and ionic strength of the solution, using values of the salting out coefficients in [33]. The activity of  $CO_2$  was estimated using the correlation of [34].

Equilibrium constants were calculated using SUPCRT92 and the slop98 database [35]. However, for  $CO_2$  where the temperature was below 100 °C, the equilibrium constant was calculated using partial molar volumes of [36]. Compared to laboratory-reported data [30, 37-41], the estimated solubility of pure gas of  $H_2$ ,  $CH_4$ ,  $CO_2$  and  $N_2$  in water has less than 5% error, except for cases of high temperature ( $\geq 200$  °C) of  $H_2$  and  $CH_4$  gases (Figure S1-S4).

## Thermophysical properties of the gas phase

### Density

Densities of pure gas or gas mixtures were estimated from SRK EOS as follows:

$$\rho_{g,i} = \frac{P_i MW_i}{Z_g RT} \quad i = H_2, CH_4, CO_2, N_2 \text{ or water vapor} \quad (3)$$

And

$$\rho_g = \sum_{i=1}^{NK+1} \rho_{g,i} \quad (4)$$

where  $\rho_{g,i}$  is the gas density of component  $i$ ;  $P_i$  is the partial pressure of component  $i$ ;  $MW_i$  is the molecular weight of component  $i$ ;  $Z_g$  is the gas compressibility factor;  $R$  is the gas constant;  $T$  is temperature and  $\rho_g$  is the gas density of gas mixtures.

The model provides accurate density estimations against NIST values for the single gas of  $H_2$ ,  $CH_4$  and  $N_2$  [8], with the maximum error of less than 1%. However, the model generally underestimates  $CO_2$  density for low-temperature ( $< 100$  °C) cases, with the maximum error up to 30% at a pressure of around 100 bar (Figures S1-S4).

## Viscosity

Viscosities of the pure gas or gas mixtures were calculated from the correlation developed from the friction theory in conjunction with the SRK EOS [42-44], as follows:

$$\eta = \eta_0 + \eta_f \quad (5)$$

where  $\eta_0$  is the dilute gas viscosity term and  $\eta_f$  is a residual fraction viscosity term. The dilute gas viscosity term is calculated by Chung et al.'s model [45] as:

$$\eta_{0,i} = 40.785 \frac{\sqrt{MW_i T}}{v_{c,i}^{2/3} \Omega_i^*} F_{c,i} \quad (6)$$

where  $\eta_{0,i}$  is the dilute gas term of component  $i$ , and  $v_{c,i}$  is the critical volume of component  $i$ , and  $F_{c,i}$  for a nonpolar gas is:

$$F_{c,i} = 1 - 0.2756\omega_i \quad (7)$$

where  $\omega_i$  is the acentric factor of component  $i$ . The reduced collision integral  $\Omega_i^*$  of component  $i$  corresponds to

$$\begin{aligned} \Omega_i^* = & \frac{1.16145}{T_i^{*0.14874}} + \frac{0.52487}{\exp(0.7732T_i^*)} + \frac{2.16178}{\exp(2.43787T_i^*)} \\ & - 6.435 \times 10^{-4} T_i^{*0.14874} \sin(18.0323T_i^{*-0.7683} - 7.27371) \end{aligned} \quad (8)$$

with

$$T_i^* = \frac{1.2593T}{T_{c,i}} \quad (9)$$

where  $T_{c,i}$  is the critical temperature of component  $i$ . For gas mixtures, the dilute gas viscosity term is calculated using the Wilke mixing rule [46] as

$$\eta_0 = \frac{\sum_{i=1}^{NK} y_i \eta_{0,i}}{\sum_{j=1}^{NK} y_j \Phi_{i,j}} \quad (10)$$

with

$$\Phi_{i,j} = \frac{\left[ 1 + \left( \frac{\eta_{0,i}}{\eta_{0,j}} \right)^{0.5} \left( \frac{MW_j}{MW_i} \right)^{0.5} \right]^2}{\frac{4}{\sqrt{2}} \left[ 1 + \frac{MW_i}{MW_j} \right]^{0.5}} \quad (11)$$

According to the friction theory, the residual friction term of an NK-component can be estimated as

$$\eta_f = k_r p_r + k_a p_a + k_{rr} p_r^2 \quad (12)$$

where  $p_a$  and  $p_r$  are the repulsive and attractive pressures that are calculated using SKR EOS. For light gas mixtures, friction constants  $k_r$ ,  $k_a$  and  $k_{rr}$  can be estimated using the linear mixing rules

$$k_r = \sum_{i=1}^{NK} y_i \kappa_{r,i}, k_a = \sum_{i=1}^{NK} y_i \kappa_{a,i} \text{ and } k_{rr} = \sum_{i=1}^{NK} y_i \kappa_{rr,i} \quad (13)$$

where  $\kappa_{r,i}$ ,  $\kappa_{a,i}$  and  $\kappa_{rr,i}$  are the friction coefficients of the pure component  $i$ . The friction coefficients of H<sub>2</sub>, CH<sub>4</sub> and N<sub>2</sub> were calculated using friction constants through the regression [44, 47]. For CO<sub>2</sub>, the friction coefficients were estimated from the general one-parameter model [42].

Compared to NIST values, the model underestimates the dynamic viscosity of H<sub>2</sub>, CH<sub>4</sub>, N<sub>2</sub> and CO<sub>2</sub> in high-pressure cases, by using the friction coefficient values of each pure component provided by [44]. Model calibration, by adjusting the friction coefficient values and by increasing the dilute gas term by 11%, gives less than 1% error for pure CH<sub>4</sub>, N<sub>2</sub> and CO<sub>2</sub> gases. However, higher errors up to 5% were found for pure H<sub>2</sub> gas in the case of high temperature and pressure (e.g., T ≥ 150 °C and P = 1000 bar) (Figures S1-S4). Further verification of the model against lab measurements of H<sub>2</sub>-CH<sub>4</sub> gas mixtures resulted in accurate viscosity estimations, with the maximum error of 2% (Figure 1).

## Enthalpy

Enthalpy of a single gas or a gas mixture ( $H_g^{T,p}$ ) was calculated as the summation of three quantities [48], as below:

$$H_g^{T,p} = [H_g(T,p) - H_g(T,p^0)] + \sum_{i=1}^{NK} y_i \{ [H_g^i(T,p^0) - H_g^i(T^0,p^0)] + H_g^i(T^0,p^0) \} \quad (14)$$

where  $[H_g(T,p) - H_g(T,p^0)]$  is the enthalpy departure at the reference pressure ( $p^0$ ) for a single gas or a gas mixture;  $X_i$  is the mass fraction for component  $i$ ;  $[H_g^i(T,p^0) - H_g^i(T^0,p^0)]$  is the ideal gas enthalpy difference for the reference temperature ( $T^0$ ) for component  $i$ ;  $H_g^i(T^0,p^0)$  is the enthalpy at the reference state for component  $i$ .

The enthalpy departure of the gas phase can be calculated using the SRK EOS:

$$[H_g(T,p) - H_g(T,p^0)] = RT \left\{ (Z_g - 1) - \frac{A}{B} \left[ 1 + \frac{T}{\alpha} \left( \frac{d\alpha}{dT} \right) \right] \ln \left( 1 + \frac{B}{Z_g} \right) \right\} \quad (15)$$

For a single gas phase of component  $i$

$$\frac{T}{\alpha} \left( \frac{d\alpha}{dT} \right) = 1 + m_i \sqrt{\frac{T}{T_{c,i} \alpha_i}} \quad (16)$$

With

$$m_i = 0.48508 + 1.55171\omega_i - 0.15613\omega_i^2 \quad (17)$$

$$\alpha_i = \left[ 1 + m_i \left( 1 - \sqrt{\frac{T}{T_{c,i}}} \right) \right]^2 \quad (18)$$

For a gas mixture of NK components

$$\frac{T}{\alpha} \left( \frac{d\alpha}{dT} \right) = \frac{\sum_{i=1}^{NK} \sum_{j=1}^{NK} y_i y_j m_j (1 - k_{ij\_SRK}) \sqrt{a_i \alpha_i a_j \frac{T}{T_{c,j}}}}{\sum_{i=1}^{NK} \sum_{j=1}^{NK} y_i y_j (1 - k_{ij\_SRK}) a_i \alpha_i a_j} \quad (19)$$

With

$$a_i = 0.42747 \frac{R^2 T_{c,i}^2}{p_{c,i}} \quad (20)$$

where  $k_{ij\_SRK}$  is the binary interaction coefficient for SRK EOS. Details of the calculations of A and B can be found in [28].

The ideal gas enthalpy difference for the reference temperature ( $T^0$ ) for component  $i$  was calculated by integrating the specific heat capacity ( $C_g$ ):

$$[H_g^i(T,p^0) - h_g^i(T^0,p^0)] = R \int_{T^0}^T C_g^i dT \quad (21)$$

where  $C_g^i$  is a function of the temperature of component  $i$  according to the following fourth order polynomial equation:

$$C_g^i = C_{g,1}^i + C_{g,2}^i T + C_{g,3}^i T^2 + C_{g,4}^i T^3 + C_{g,5}^i T^4 \quad (22)$$

where  $C_{g,1}^i$  to  $C_{g,5}^i$  are coefficients [49]. The temperature of the triple point of water ( $T^0=273.16$  and  $p^0=611.73$  Pa) was considered as the reference state. The enthalpy at the reference state for component  $i$  was obtained from the NIST website[8]. The model provides accurate enthalpy estimations against NIST values for the single gas of  $H_2$ ,  $CH_4$ ,  $N_2$  and  $CO_2$ , with the maximum error of less than 1% (Figures S1-S4).

### Numerical schemes

GPSFLOW uses the conventional integrated finite difference method to discretize the conservation of mass and energy equations (Table 1) in space. Time is discretized as a first-order finite difference. These result in strong coupled and non-linear algebraic equations. To obtain the numerical stability for solving these non-linear algebraic equations, three numerical approaches can be chosen according to the grid blocks: 1) The fully implicit method (FIM) uses Newton-Raphson iterations to solve pressure and saturation simultaneously which is similar to TOUGH3 [17]; 2) The implicit pressure explicit saturation (IMPES) method solves pressure implicitly and then calculates saturation based on pressure solutions; 3) The adaptive implicit method (AIM) solves saturation and pressure implicitly in the regions where large variations in the saturation occur and uses IMPES for other regions [50]. Each time step involves the calculation of a Jacobian matrix and the solution of a set of linear equations, with automatic adjustment of the size of each time step according to the convergence rate of the iteration process.

GPSFLOW assumes that locally all phases are in thermodynamic equilibrium. Pressure, temperature, gas saturation (if two-phase) and non-water components are used as the primary variables, which represent the unknowns to be calculated in each time step. Therefore, the equation of the pressure is not specified but is instead introduced in the mass balance equation via Darcy's law. For single flow, the continuity of the existing phase determines the pressure. For two-phase flow, the gas phase determines the pressure. In addition, the liquid is treated as incompressible.

### Numerical solvers

Solving linear equations is the most time-consuming task for a numerical model. GPSFLOW uses a standard distributed compressed sparse row format for storage of a Jacobian matrix and right-hand side vector. This provides great flexibility for calling third-party linear solvers. Currently, GPSFLOW has an interface with the solver packages including AMGCL-best for FIM, shared memory and GPU or hybrid parallel computing [51], PETSC-best for extremely large-scale simulation with MPI parallel computing [52, 53]), TRILINOs-best for large-scale model simulation with hybrid parallel computing [54], AMGX-best for huge models on super computers equipped with multiple CUDA GPUs [55], rocAlution-best for running on super-computers with AMD type GPUs for huge models [56], etc.

### Parallel computing schemes

GPSFLOW uses the domain decomposition method together with OPENMP for the implementation of hybrid parallel computing simulations. This is done by using ParMETIS for parallel modelling domain partition to achieve the balance of computational tasks, memory requirement and communication volume among the participating CPUs [57]. An advanced local and global variables communication scheme was designed using MPI. This also ensures thread-safe in OPENMP multi-thread parallel computing, which is implemented by using a large loop for the assembly of a Jacobian matrix and EOS computation. In addition, the GPU parallelization for solving linear equations can

also be done through using GPU-supported linear solvers. These advanced parallel computing techniques enable the simulation to be run on a multi-core PC, workstation, and high-performance computing facility.

## Verification, evaluations and application

### Verification: 1D non-isothermal radial flow of H<sub>2</sub> in a synthetic aquifer

To verify the accuracy of GPSFLOW, a 1D radial flow of H<sub>2</sub> in a synthetic aquifer was run using both GPSFLOW and TOUGH/EWAGS module [17]. TOUGH/EWAGS module is capable of modelling H<sub>2</sub> single gas flow in an aquifer based on the ideal gas law and has been recently used for assessing H<sub>2</sub> injection and withdrawal at a deep aquifer in Poland [13]. In this 1 D radial model of infinite extent with 20 grid blocks in total, H<sub>2</sub> is injected for 100 days at a constant rate of 0.24 kg/s. The aquifer is homogeneous with a permeability of 10<sup>-12</sup> m<sup>2</sup> and porosity of 0.35 and has a thickness of 10 m. The initial pressure of the aquifer is 150 bar and initial temperature is 65 °C. Figure 2 compares the pressure, gas saturation, mass fraction of H<sub>2</sub> and H<sub>2</sub> density in the gas phase obtained from two simulators. GPSFLOW yields the same results for gas saturation and mass fraction of H<sub>2</sub> as the TOUGH/EWAGS module. However, there are some discrepancies for gas pressure and density. This is expected, as TOUGH/EWAGS uses the ideal gas law to calculate the thermophysical property (density, viscosity, etc.) but GPSFLOW uses the real gas law. In high-pressure cases, H<sub>2</sub> gas does not completely obey the ideal gas law. This inevitably leads to slight differences between these two simulators. Overall, the comparison with TOUGH/EWAGS verifies the accuracy of GPSFLOW in modelling pure hydrogen storage in deep aquifers. A single core was used for the simulation, with 79 time steps (the elapsed time: 0.13 seconds).

### Evaluations

#### H<sub>2</sub> storage in salt caverns

To evaluate non-isothermal gas storage in salt caverns, GPSFLOW was used to simulate H<sub>2</sub> injection/withdrawal in a synthetic cavern. The synthetic cavern had a roof depth of 600 m below ground surface, which is similar to the caverns at the Huntorf compressed air energy storage used for modelling by [58] and the salt cavern at Teesside, England currently used for H<sub>2</sub> storage [9]. The cavern was set up as a cylinder with a diameter of ~9 m and a height of 100 m with a total volume of ~7200 m<sup>3</sup>. The salt cavern was treated as a homogenous porous media with a permeability of 10<sup>-12</sup> m<sup>2</sup>, porosity of 0.99, thermal conductivity of 0.18 W m<sup>-1</sup> K<sup>-1</sup> and specific heat of 14.6 kJ kg<sup>-1</sup> K<sup>-1</sup>. The model lateral boundary in the salt formation was 15 m from the cavern with no flow boundary. The salt rock was assumed to be homogenous, with a permeability of 10<sup>-16</sup> m<sup>2</sup>, porosity of 0.2, thermal conductivity of 2.1 W m<sup>-1</sup> K<sup>-1</sup> and specific heat of 1 kJ kg<sup>-1</sup> K<sup>-1</sup>. Hydrostatic pressure (60-70 bar) was assigned as initial pressure of the cavern and salt rock, with an initial temperature of ~35 °C. The salt cavern was initially saturated with H<sub>2</sub> gas. A daily injection and production cycle was used for the simulation, with 12-hour H<sub>2</sub> injection of 0.1 kg s<sup>-1</sup>, 3.5-hour shut-in and 3-hour production of 0.4 kg s<sup>-1</sup>. The cavern and surrounding rock were discretized into 1,200 grid blocks with 12 vertical layers. The simulation was run for 10 cycles (days). In this evaluation, the Darcy model was used to estimate the gas velocity within the cavern. This is because, with the injection and production rates above, the normalised hydrogen mass change rate to total hydrogen mass in the cavern is small and insignificant (~5 X10<sup>-5</sup> s<sup>-1</sup>). A similar approach has also been used to model compressed air energy storage in caverns at Huntorf [58].

Figure 3 shows the injection/production cycle and its corresponding pressure and temperature within the synthetic cavern as well as temperature, pressure and gas saturation along the radial distance at the end of the simulation. The simulation results show that pressure and temperature

within the cavern correspond to the injection and production cycle, with increased pressure and temperature during the injection period and vice versa during the production period (Figure 3a). Gas saturation, temperature and pressures profiles along the radial distance at the end of the simulation suggest that the increased gas pressure and temperature in the cavern might have an impact on the surrounding rock but that migration of H<sub>2</sub> gas within the salt formation is limited (Figure 3b). As the stability of salt caverns and the mechanical behaviour of the surrounding rock material are sensitive to pressure and temperature fluctuations during periods of gas import and export, the modelling results suggest that GPSFLOW can be used to assess how the operating regime of H<sub>2</sub> storage will impact the cavern integrity over its predicted lifetime. This could help to design an optimal operating regime to meet the storage demand and minimize the impact on cavern integrity. The simulation was run on a multi-core PC. Four cores were used in the simulation with 1,070 time steps (the elapsed time: 34.09 seconds).

### H<sub>2</sub> injection in a 1D CH<sub>4</sub> saturated aquifer experiment

To evaluate GPSFLOW modelling capacity for the gas mixture system, the model was applied to model each H<sub>2</sub> and CO<sub>2</sub> injection into a methane-saturated aquifer. The methane-saturated aquifer was a 0.3048 m (1 foot wide) by 0.3048 m (1 foot high) by 61 m (200 feet long), which was originally constructed to investigate CO<sub>2</sub> injection in a methane-saturated horizontal column [59]. The experiment was discretized into 122 grid blocks (0.5 m for each grid block in the horizontal direction). Dry CO<sub>2</sub> was injected into the column from the left and gas and liquid exited from the right at constant pressure. The experiment has also been used for modelling by [60] and the parameters of the problem are listed in Table 2. In this evaluation, GPSFLOW was used to simulate dry H<sub>2</sub> injection in the methane-saturated aquifer with an injection rate of  $9.4 \times 10^{-4} \text{ kg s}^{-1}$  and  $2.16 \times 10^{-5} \text{ kg s}^{-1}$ . The smaller H<sub>2</sub> injection rate of the later was used to ensure a similar volumetric injection rate as the experimental CO<sub>2</sub> injection rate of  $9.4 \times 10^{-4} \text{ kg s}^{-1}$ . For comparison, GPSFLOW was also used to simulate the laboratory CO<sub>2</sub> injection.

Figure 4 shows pressure, gas saturation and density as well as mass fractions of H<sub>2</sub>, CO<sub>2</sub>, CH<sub>4</sub> and water vapour along the horizontal column at a simulation time of 1 day. The results indicate that, with the H<sub>2</sub> injection rate of  $9.4 \times 10^{-4} \text{ kg s}^{-1}$  the same as CO<sub>2</sub> in the experiment, H<sub>2</sub> displaces CH<sub>4</sub>-saturated water and produces a bank of H<sub>2</sub> gas in the whole column. However, when H<sub>2</sub> injection at a volumetric injection rate ( $2.16 \times 10^{-5} \text{ kg s}^{-1}$  as the CO<sub>2</sub> density is 53.5 times greater than H<sub>2</sub> at P = 200 bar and T = 91.8 °C, NIST, 2021) similar to the CO<sub>2</sub> rate, H<sub>2</sub> displaces CH<sub>4</sub>-saturated water and produces a bank of H<sub>2</sub> gas at the gas-phase front at the column distance of ~23 m but CO<sub>2</sub> at ~18 m (Figure 4a). As expected, GPSFLOW shows that H<sub>2</sub> is more mobile than CO<sub>2</sub>. This is because the viscosity of H<sub>2</sub> is ~4 times less than that of CO<sub>2</sub> under these experimental conditions. Meanwhile, lighter density and lower viscosity of H<sub>2</sub> gas also formed an over 10 m H<sub>2</sub>-CH<sub>4</sub> gas mixture at the H<sub>2</sub> injection front, while a less than 5 m H<sub>2</sub>-CO<sub>2</sub> mixture was found for CO<sub>2</sub> injection (Figure 4b). Gas densities of H<sub>2</sub> and CO<sub>2</sub> estimated by GPSFLOW match the NIST data well (<5%). In addition, the model estimated a mass fraction of water vapour in the gas phase of about 2% for H<sub>2</sub>, which is much higher than ~0.2% in the CO<sub>2</sub> gas phase (Figure 4c). This is mainly due to the low density of H<sub>2</sub>. Overall, the evaluation of GPSFLOW against the experimental injection shows that the model is capable of modelling H<sub>2</sub> and/or CO<sub>2</sub> injection in CH<sub>4</sub>-saturated aquifers, which is similar to the conditions in depleted gas fields. A single core was used for these simulations, with ~25 time steps for each simulation (the elapsed time: 0.07 seconds).

## Application: H<sub>2</sub> storage in a depleted gas field using CO<sub>2</sub> as a cushion gas

### H<sub>2</sub> injection

To evaluate the applicability of GPSFLOW in relation to reservoir conditions, simulations of H<sub>2</sub> and CO<sub>2</sub> injections were conducted at the Rio Vista Gas Field. Rio Vista was the largest gas field in California and has produced over  $9.3 \times 10^{10}$  m<sup>3</sup> of natural gas since 1936 (under standard conditions of 1 bar and 15.5 °C) [61]. Rio Vista is located approximately 75 km northeast of San Francisco. It has an elongated dome-shaped structure extending over an area of 12 km by 15 km. The most productive pool in the Domengine formation occurs at an average depth of 1,150 to 1,310 m with an average net thickness of 15 to 100 m. The initial reservoir pressure and temperature were approximately 120 bar and 65 °C. A simplified 2-D model system based on the Rio Vista and corresponding to 1/16 of the actual length of the reservoir was constructed. The TOUGH/EOS7C module was used to simulate the withdrawal of CH<sub>4</sub> at the historical rate first. The end of the production was then used as initial conditions for CO<sub>2</sub> injection simulation [62]. The model system was a 1-km-wide cross-section with vertical dimensions of 100 m and horizontal extent of 6,600 m of the western flank of the dome. The model reservoir has a roof sloping at 0.78 degrees to the west and is discretized into 660 grid blocks (33 in the horizontal direction and 20 in the vertical direction). The properties of the formation and other parameters have been detailed in [62].

Figure 5 shows the mass fraction in the gas phase for three gas injection scenarios simulated by GPSFLOW. Scenario 1 assumed H<sub>2</sub> injection of 0.33 kg H<sub>2</sub>/s, which is similar to a volumetric injection rate of CO<sub>2</sub> in 8.2 kg CO<sub>2</sub> s<sup>-1</sup> applied by Oldenburg et al. [62] using the end of CH<sub>4</sub> withdrawal as initial conditions. H<sub>2</sub> gas mass fractions after 1 year and 10 years of injection are shown in Figure 5a & 5b, respectively. Scenario 2 assumed a H<sub>2</sub> mass injection rate (8.2 kg H<sub>2</sub>/s) which is the same as the CO<sub>2</sub> mass injection rate for 1 year (Figure 5c). Scenario 3 simulated the same CO<sub>2</sub> mass injection rate as that conducted by [62] for comparison (Figure 5d). Modelled results show that, with the same volumetric injection as CO<sub>2</sub> for 10 years, H<sub>2</sub> occupies less space of the gas field than CO<sub>2</sub> and high H<sub>2</sub> gas mass fraction mainly distributes close to the caprock due to the buoyancy of CH<sub>4</sub> (higher density of CH<sub>4</sub> than H<sub>2</sub>). In Scenario 2, H<sub>2</sub> almost occupied the entire reservoir and depressed the water table below the injection point after one year of injection. This is because H<sub>2</sub> density is an order of magnitude less than CO<sub>2</sub> but the same H<sub>2</sub> mass injection rate as CO<sub>2</sub> was applied for the investigation. In Scenario 3, the simulation of the CO<sub>2</sub> injection produced a contour of CO<sub>2</sub> mass fraction in the gas phase, which is similar to the results simulated by TOUGH/EOS7C [17, 60]. Overall, the simulations show that GPSFLOW is capable of modelling H<sub>2</sub> injection in depleted gas fields. A single core was used for these simulations, with ~430 time steps for each simulation (the elapsed time: 12.3 seconds).

### H<sub>2</sub> storage using CO<sub>2</sub> as cushion gas

To further evaluate GPSFLOW modelling capability, the 2-D simplified Rio Vista model was extended to the right-hand side symmetrically to form a synthetic anticline with 1,320 grid blocks. We simulated CO<sub>2</sub> injection at two points: Point one 15 m below the top of the reservoir at the horizontal distance of 2,000 m as in the previous tests and Point two at the same depth but at the horizontal distance of 11,000 m. In addition, a third point (Point three) 38 m below the top of the reservoir at the horizontal distance of 6,600 m was used for CH<sub>4</sub> withdrawal and H<sub>2</sub> injection/production (Figure 7a).

The simulation of CO<sub>2</sub> injection as a cushion gas and enhanced CH<sub>4</sub> recovery, H<sub>2</sub> bubble development and annual H<sub>2</sub> injection and production cycle are shown in Figure 6a. The timeline of the simulation was: 1) Years 1-10: CO<sub>2</sub> injection at a rate of 8.2 kg/s at Points one and two; 2) Years 7-10: CH<sub>4</sub> production at a rate of 8.2 kg/s at Point three. The selection of the CO<sub>2</sub> injection and subsequent CH<sub>4</sub>

production mode, instead of the simultaneous CO<sub>2</sub> injection and CH<sub>4</sub> production mode, was to minimize CO<sub>2</sub> in the production well as suggested by [60]; 3) Year 11: H<sub>2</sub> bubble development with H<sub>2</sub> injection at a rate of 4 kg/s for 9 months followed by 3-month production at a rate of 1 kg/s at Point three; 4) Years 12-20: H<sub>2</sub> injection/production cycle with H<sub>2</sub> injection at a rate of 1 kg/s for 6 months, shut-in for 3 months and a production rate of 1 kg/s for 3 months each year; 5) Years 21-30: the gas storage shut-ins for 10 year.

The simulation results show that CO<sub>2</sub> injection repressurizes the reservoir while CH<sub>4</sub> production depressurizes the reservoir. H<sub>2</sub> bubble development then repressurizes the gas reservoir. During the H<sub>2</sub> injection/production cycle, the pressure in the reservoir slightly increases but remains stable during the shut-in period from Years 21 to 30. There is no CO<sub>2</sub> in the production well. However, there is an increase of CH<sub>4</sub> mass fraction in the production well with the production time and the increased number of cycles. The CH<sub>4</sub> mass fraction in the production well is less than 10% in the first cycle rising to ~40% at the last cycle (Figure 6b). This is due to the increased H<sub>2</sub>-CH<sub>4</sub> mixture at the end of the production period. Overall, there are over 5 million tonnes of CO<sub>2</sub> storage in the gas reservoir, about 1 million tonnes of CH<sub>4</sub> production and over 125,000 tonnes of H<sub>2</sub> storage in the reservoir by the end of the H<sub>2</sub> injection and production cycle (Figure 6c).

Pressure and mass fraction distributions of CO<sub>2</sub>, CH<sub>4</sub> and H<sub>2</sub> by the end of Year 11 show that the CO<sub>2</sub> injection from both sides pushes the CH<sub>4</sub> to the centre of the domain, and there is a H<sub>2</sub> bubble surrounded by CH<sub>4</sub> at the centre of the domain (Figure 7). This confirms that the CO<sub>2</sub> injection repressurizes the reservoir to enhance CH<sub>4</sub> recovery and H<sub>2</sub> injection at the centre of the domain which can ensure that CH<sub>4</sub> acts as a cushion gas for H<sub>2</sub> storage and prevents CO<sub>2</sub>-H<sub>2</sub> mixture during the gas production. Comparisons of mass fractions of CO<sub>2</sub>, CH<sub>4</sub> and H<sub>2</sub> by the end of Year 11 and Year 20 indicate that, due to the density stratification as driven by density and pressure gradients, CO<sub>2</sub> at both sides of the domain migrates downward as does CH<sub>4</sub> at the centre of the domain. In addition, the buoyancy of CH<sub>4</sub> drives H<sub>2</sub> bubbles to migrate upward, which leads to an increase of CH<sub>4</sub> mass fraction in the production point (Figure 8). A single core was used for the simulations, with ~880 time steps (the elapsed time: 75.9 seconds).

## Conclusion

Modelling capability for the robust simulator (GPSFLOW) has been extended for modelling grid-scale hydrogen and gas mixture (H<sub>2</sub>-CO<sub>2</sub>-CH<sub>4</sub>-N<sub>2</sub>) subsurface storage. With the new non-iterative activity-fugacity thermodynamic model, estimated solubility, density, viscosity, and enthalpy of pure gas or gas mixtures by GPSFLOW are in good agreement with NIST thermophysical data and reported experimental data, over a range of temperatures from 20-200 °C and pressure up to 1000 bar.

GPSFLOW has been benchmarked with a single gas model of TOUGH2/EWASG for hydrogen storage in a synthetic aquifer experiment, as well as with TOUGH2/EOS7c for CO<sub>2</sub> storage in a depleted gas field. Applications of GPSFLOW for simulating H<sub>2</sub> storage in a salt cavern, H<sub>2</sub> injection into a CH<sub>4</sub>-saturated aquifer experiment, and hydrogen storage in a depleted gas field using CO<sub>2</sub> as a cushion gas and for enhanced natural gas recovery demonstrate its capability of simulating different underground hydrogen storage scenarios. The results show that GPSFLOW is capable of modelling non-isothermal, multiphase and multicomponent flow in H<sub>2</sub>-water, H<sub>2</sub>-CH<sub>4</sub>-water, and H<sub>2</sub>-CH<sub>4</sub>-CO<sub>2</sub>-water systems at high pressure and temperature. With the application of advanced parallel computing techniques, GPSFLOW offers a robust numerical tool to model subsurface hydrogen storage and gas mixture at reservoir scale on a multi-core PC, workstation, and high-performance computing facility. The simulator is available for evaluation upon request.

## **Acknowledgement**

The authors would like to thank the subject editor (Dr. Milos B Djukic) and four anonymous reviewers' comments regarding improvement of the manuscript. The work is partly funded by the Royal Academy of Engineer through industrial fellowship scheme, Award number: IF2122\171 to the first author.

## References

- [1] IEA. NET Zero by 2050-A Roadmap for the Global Energy Sector. France: International Energy Agency; 2021.
- [2] Committee on Climate Change. Net Zero - The UK's contribution to stopping global warming. London 2019.
- [3] National Grid. Future Grid: Insight and innovation. 2020.
- [4] Wallace RL, Cai ZS, Zhang HX, Zhang KN, Guo CB. Utility-scale subsurface hydrogen storage: UK perspectives and technology. *International Journal of Hydrogen Energy*. 2021;46:25137-59.
- [5] Caglayan DG, Weber N, Heinrichs HU, Linssen J, Robinius M, Kukla PA, et al. Technical potential of salt caverns for hydrogen storage in Europe. *International Journal of Hydrogen Energy*. 2020;45:6793-805.
- [6] Pellow MA, Emmott CJM, Barnhart CJ, Benson SM. Hydrogen or batteries for grid storage? A net energy analysis. *Energy & Environmental Science*. 2015;8:1938-52.
- [7] Tarkowski R. Underground hydrogen storage: Characteristics and prospects. *Renewable & Sustainable Energy Reviews*. 2019;105:86-94.
- [8] NIST. Thermophysical Properties of Fluid Systems. 2021.
- [9] ATKINS. Salt Cavern Appraisal for Hydrogen and Gas Storage. London 2018.
- [10] Budak P, Szpunar T. How does the composition of natural gas/hydrogen mixture fluctuate during exploitation of a gas cavern. *Nafta-Gaz*. 2020:799-806.
- [11] Pinto JSR, Bachaud P, Fargetton T, Ferrando N, Jeannin L, Louvet F. Modeling phase equilibrium of hydrogen and natural gas in brines: Application to storage in salt caverns. *International Journal of Hydrogen Energy*. 2021;46:4229-40.
- [12] Heinemann N, Scafidi J, Pickup G, Thaysen EM, Hassanouryouzband A, Wilkinson M, et al. Hydrogen storage in saline aquifers: The role of cushion gas for injection and production. *International Journal of Hydrogen Energy*. 2021;46:13.
- [13] Lubon K, Tarkowski R. Numerical simulation of hydrogen injection and withdrawal to and from a deep aquifer in NW Poland. *International Journal of Hydrogen Energy*. 2020;45:2068-83.
- [14] Sainz-Garcia A, Abarca E, Rubi V, Grandia F. Assessment of feasible strategies for seasonal underground hydrogen storage in a saline aquifer. *International Journal of Hydrogen Energy*. 2017;42:16657-66.
- [15] Pfeiffer WT, Beyer C, Bauer S. Hydrogen storage in a heterogeneous sandstone formation: dimensioning and induced hydraulic effects. *Petroleum Geoscience*. 2017;23:315-26.
- [16] Flemisch B, Darcis M, Erbertseder K, Faigle B, Lauser A, Mosthaf K, et al. DuMu(x): DUNE for multi-{phase, component, scale, physics, ...}flow and transport in porous media. *Advances in Water Resources*. 2011;34:1102-12.
- [17] Jung Y, Pau GSH, Finsterle S, Doughty C. TOUGH3 User's Guide. Berkeley, California: Energy Geosciences Division, University of California; 2018.
- [18] Pfeiffer WT, Graupner B, Bauer S. The coupled non-isothermal, multiphase-multicomponent flow and reactive transport simulator OpenGeoSys-ECLIPSE for porous media gas storage. *Environmental Earth Sciences*. 2016;75.
- [19] RAG. RAG Austria AG-UNDERGROUND SUN STORAGE: Chemical storage of renewable energy in porous subsurface reservoirs with exemplary testbed. 2020.
- [20] Lysy M, Ferno M, Ersland G. Seasonal hydrogen storage in a depleted oil and gas field. *International Journal of Hydrogen Energy*. 2021;46:25160-74.
- [21] Moridis GJ, Freeman CM. The RealGas and RealGasH2O options of the TOUGH plus code for the simulation of coupled fluid and heat flow in tight/shale gas systems. *Computers & Geosciences*. 2014;65:56-71.
- [22] Zhang K. User's Guide for GPSFlow-A hybrid parallel computing general purpose subsurface flow simulator. Danville, California Tough Modelling Group; 2021.

- [23] Kolditz O, Bauer S, Bilke L, Bottcher N, Delfs JO, Fischer T, et al. OpenGeoSys: an open-source initiative for numerical simulation of thermo-hydro-mechanical/chemical (THM/C) processes in porous media. *Environmental Earth Sciences*. 2012;67:589-99.
- [24] Wu YS. A virtual node method for handling well bore boundary conditions in modeling multiphase flow in porous and fractured media. *Water Resources Research*. 2000;36:807-14.
- [25] Oldenburg CM, Moridis GJ, Spycher N, Pruess K. EOS7c Version 1.0: TOUGH2 Module for Carbon Dioxide or Nitrogen in Natural Gas (Methane) Reservoirs Berkeley, CA 94720: Earth Science Division, Lawrence Berkeley National Laboratory, University of California; 2004.
- [26] Oldenburg CM. EOS7CA Version 1.0: TOUGH2 Module for Gas Migration in Shallow Subsurface Porous Media Systems. Berkeley, CA 94720: Earth Sciences Division, Lawrence Berkeley National Laboratory, University of California; 2015.
- [27] Shabani B, Vilcaez J. A fast and robust TOUGH2 module to simulate geological CO<sub>2</sub> storage in saline aquifers. *Computers & Geosciences*. 2018;111:58-66.
- [28] Soave G. EQUILIBRIUM CONSTANTS FROM A MODIFIED REDLICH-KWONG EQUATION OF STATE. *Chemical Engineering Science*. 1972;27:1197-&.
- [29] Knapp H, Döring R, Oellrich L, Plöcke V, Prausnitz JM. Vapor—Liquid Equilibria for Mixtures of Low Boiling Substances. Frankfurt am Main 1982.
- [30] Rahbari A, Brenkman J, Hens R, Ramdin M, van den Broeke LJP, Schoon R, et al. Solubility of Water in Hydrogen at High Pressures: A Molecular Simulation Study. *Journal of Chemical and Engineering Data*. 2019;64:4103-15.
- [31] Valderrama JO, Cisternas LA, Vergara ME, Bosse MA. BINARY INTERACTION PARAMETERS IN CUBIC EQUATIONS OF STATE FOR HYDROGEN HYDROCARBON MIXTURES. *Chemical Engineering Science*. 1990;45:49-54.
- [32] Walas SW. *Phase Equilibria in Chemical Engineering*. Boston, MA, USA: Butterworth; 1985.
- [33] Langmuir D. *Aqueous Environmental Geochemistry*. Upper Saddle River, New Jersey 07458: Prentice Hall, Inc.; 1997.
- [34] Drummond SE. *Boiling and mixing of hydrothermal fluids — Chemical effects on mineral precipitation: Pennsylvania State University* 1981.
- [35] Johnson JW, Oelkers EH, Helgeson HC. SUPCRT92 - A SOFTWARE PACKAGE FOR CALCULATING THE STANDARD MOLAL THERMODYNAMIC PROPERTIES OF MINERALS, GASES, AQUEOUS SPECIES, AND REACTIONS FROM 1-BAR TO 5000-BAR AND 0-DEGREES-C TO 1000-DEGREES-C. *Computers & Geosciences*. 1992;18:899-947.
- [36] Spycher N, Pruess K, Ennis-King J. CO<sub>2</sub>-H<sub>2</sub>O mixtures in the geological sequestration of CO<sub>2</sub>. I. Assessment and calculation of mutual solubilities from 12 to 100 degrees C and up to 600 bar. *Geochimica Et Cosmochimica Acta*. 2003;67:3015-31.
- [37] Chabab S, Theveneau P, Coquelet C, Corvisier J, Paricaud P. Measurements and predictive models of high- pressure H<sub>2</sub> solubility in brine (H<sub>2</sub>O+NaCl) for underground hydrogen storage application. *International Journal of Hydrogen Energy*. 2020;45:32206-20.
- [38] Chapoy A, Mohammadi AH, Tohidi B, Richon D. Gas solubility measurement and modeling for the nitrogen plus water system from 274.18 K to 363.02 K. *Journal of Chemical and Engineering Data*. 2004;49:1110-5.
- [39] Hassanpouryouzband A, Farahani MV, Yang JH, Tohidi B, Chuvilin E, Istomin V, et al. Solubility of Flue Gas or Carbon Dioxide-Nitrogen Gas Mixtures in Water and Aqueous Solutions of Salts: Experimental Measurement and Thermodynamic Modeling. *Industrial & Engineering Chemistry Research*. 2019;58:3377-94.
- [40] Mohammadi AH, Chapoy A, Tohidi B, Richon D. Water content measurement and modeling in the nitrogen plus water system. *Journal of Chemical and Engineering Data*. 2005;50:541-5.
- [41] Ou WJ, Geng LT, Lu WJ, Guo HR, Qu K, Mao PX. Quantitative Raman spectroscopic investigation of geo-fluids high-pressure phase equilibria: Part II. Accurate determination of CH<sub>4</sub> solubility in water from 273 to 603 K and from 5 to 140 MPa and refining the parameters of the thermodynamic model. *Fluid Phase Equilibria*. 2015;391:18-30.

- [42] Quinones-Cisneros SE, Zeberg-Mikkelsen CK, Stenby EH. One parameter friction theory models for viscosity. *Fluid Phase Equilibria*. 2001;178:1-16.
- [43] Quinones-Cisneros SE, Zeberg-Mikkelsen CK, Stenby EH. The friction theory (f-theory) for viscosity modeling. *Fluid Phase Equilibria*. 2000;169:249-76.
- [44] Zeberg-Mikkelsen CK, Quinones-Cisneros SE, Stenby EH. Viscosity modeling of light gases at supercritical conditions using the friction theory. *Industrial & Engineering Chemistry Research*. 2001;40:3848-54.
- [45] Chung TH, Ajlan M, Lee LL, Starling KE. GENERALIZED MULTIPARAMETER CORRELATION FOR NONPOLAR AND POLAR FLUID TRANSPORT-PROPERTIES. *Industrial & Engineering Chemistry Research*. 1988;27:671-9.
- [46] Wilke CR. A VISCOSITY EQUATION FOR GAS MIXTURES. *Journal of Chemical Physics*. 1950;18:517-9.
- [47] Zeberg-Mikkelsen CK, Quinones-Cisneros SE, Stenby EH. Viscosity prediction of hydrogen plus natural gas mixtures (hythane). *Industrial & Engineering Chemistry Research*. 2001;40:2966-70.
- [48] Reid RC, Prausnitz JM, Sherwood TK. *The Properties of Gases and Liquids*. Second Edition ed. New York: McGraw-Hill Book Company,; 1977.
- [49] Poling BE, Prausnitz JM, O'connell JP. *The Properties of Gases and Liquids*. New York: McGraw-Hill 2001.
- [50] Moortgat J. Adaptive implicit finite element methods for multicomponent compressible flow in heterogeneous and fractured porous media. *Water Resources Research*. 2017;53:73-92.
- [51] Demidov D. AMGCL: an Efficient, Flexible, and Extensible Algebraic Multigrid Implementation. *Lobachevskii Journal of Mathematics* 2019;40:535-46.
- [52] Balay S, Abhyankar S, Adams MF, Brown J, Brune P, Buschelman K, et al. PETSc. 2016.
- [53] Balay S, Gropp WD, McInnes LC, Smith BF. Efficient management of parallelism in object-oriented numerical software libraries 1997.
- [54] Heroux MA, Willenbring JM. A new overview of the Trilinos project. *Scientific Programming*. 2012;20:83-8.
- [55] Naumov M, Arsaev M, Castonguay P, Cohen J, Demouth J, Eaton J, et al. AMGX: A LIBRARY FOR GPU ACCELERATED ALGEBRAIC MULTIGRID AND PRECONDITIONED ITERATIVE METHODS. *Siam Journal on Scientific Computing*. 2015;37:S602-S26.
- [56] AMD. rocALUTION. 2018.
- [57] Karypis G, Schloegel K. ParMETIS 4.0: parallel graph partitioning and sparse matrix ordering library. Minneapolis, MN, USA: Department of Computer Science and Engineering, University of Minnesota, ; 2013.
- [58] Guo CB, Pan LH, Zhang KN, Oldenburg CM, Li C, Li Y. Comparison of compressed air energy storage process in aquifers and caverns based on the Huntorf CAES plant. *Applied Energy*. 2016;181:342-56.
- [59] Taggart I. Extraction of Dissolved Methane in Brines by CO<sub>2</sub> Injection: Implication for CO<sub>2</sub> Sequestration. *Spe Reservoir Evaluation & Engineering*. 2010;13:791-804.
- [60] Oldenburg CM, Doughty C, Spycher N. The role of CO<sub>2</sub> in CH<sub>4</sub> exsolution from deep brine: Implications for geologic carbon sequestration. *Greenhouse Gases-Science and Technology*. 2013;3:359-77.
- [61] Burrough E. Rio Vista Gas Field. Summary of California oil fields. 1967. p. 25-33.
- [62] Oldenburg CM, Pruess K, Benson SM. Process modeling of CO<sub>2</sub> injection into natural gas reservoirs for carbon sequestration and enhanced gas recovery. *Energy & Fuels*. 2001;15:293-8.
- [63] Nabizadeh H, Mayinger F. Viscosity of binary mixtures of hydrogen and natural gas (hythane) in the gaseous phase. *High Temperatures-High Pressures*. 1999;31:601-12.

Table 1 The mass and energy balance equations solved in GPSFLOW.

Description	Equation	Notions
Conservation of mass and energy	$\frac{d}{dt} \int_{V_n} M^i dV_n = \int_{\Gamma_n} F^i \cdot n d\Gamma_n + \int_{V_n} q^i dV_n$	$V_n$ : an arbitrary subdomain bounded by the closed surface $\Gamma_n$ ; $M^i$ : mass or energy accumulation term of component $i$ per volume; $F$ : mass or heat flux; $n$ : normal vector on the surface element $d\Gamma_n$ pointing toward to $V_n$ ; $q$ : sink/source term of mass or energy.
Mass accumulation	$M^i = \Phi \sum_{\beta=1}^{NPH} S_{\beta} \rho_{\beta} X_{\beta}^i, i = 1, NK; \beta = 1, NPH$	$\Phi$ : porosity; $\beta$ : phase index (e.g., $\beta$ = gas, aqueous phase); $S_{\beta}$ : saturation of phase $\beta$ (the volume fractions of the pore space occupied by each phase); $\rho_{\beta}$ : density of phase $\beta$ ; $X_{\beta}^i$ : mass fraction of component $i$ in phase $\beta$ ; $NK$ : number of components; $NPH$ : number of phases.
Energy accumulation	$M^{NK+1} = \Phi \sum_{\beta=1}^{NPH} S_{\beta} \rho_{\beta} U_{\beta} + (1 - \Phi) \rho_R C_R T$	$U_{\beta}$ : specific internal energy of phase $\beta$ ; $\rho_R$ : rock density; $C_R$ : rock specific heat; $T$ : temperature.
Mass flux	$F^i = \sum_{\beta=1}^{NPH} X_{\beta}^i \rho_{\beta} u_{\beta}$	$u_{\beta}$ : Darcy's velocity (volume flux) of component $i$ in phase $\beta$ . Diffusive mass flux is ignored as it is smaller compared with advective mass flux.
Phase velocity	$u_{\beta} = -k \frac{k_{r\beta}}{\mu_{\beta}} (\nabla P_{\beta} - \rho_{\beta} g)$	$k$ : absolute permeability; $k_{r\beta}$ : relative permeability to phase $\beta$ ; $\mu_{\beta}$ : dynamic viscosity of phase $\beta$ ; $P_{\beta}$ : pressure in phase $\beta$ ( $P_{\beta} = P + P_{c\beta}$ , $P$ : pressure of gas phase; $P_{c\beta} (\leq 0)$ : capillary pressure; $g$ : gravitational acceleration
Energy flux	$F^{NK+1} = -\lambda \nabla T + \varphi \sum_{\beta=1}^{NPH} h_{\beta} \rho_{\beta} u_{\beta}$	$\lambda$ : thermal conductivity, $h_{\beta}$ : specific enthalpy in phase $\beta$ .

Table 2 Parameter values of 1D displacement column experiment [59, 60]

Property	Value
Porosity	0.25
Permeability	$1.0 \times 10^{-12} \text{ m}^2$
Capillary Pressure	0.0 Pa
Relative Permeability	Power-law, power = 2, $S_{lr} = 0.15$ and $S_{gr} = 0$
Pressure (initial and right-hand side boundary condition)	$2.04 \times 10^7 \text{ Pa}$
Temperature (isothermal)	91.8 °C
Initial aqueous phase saturation	$S_l = 1.0$
Grid spacing	0.5 m

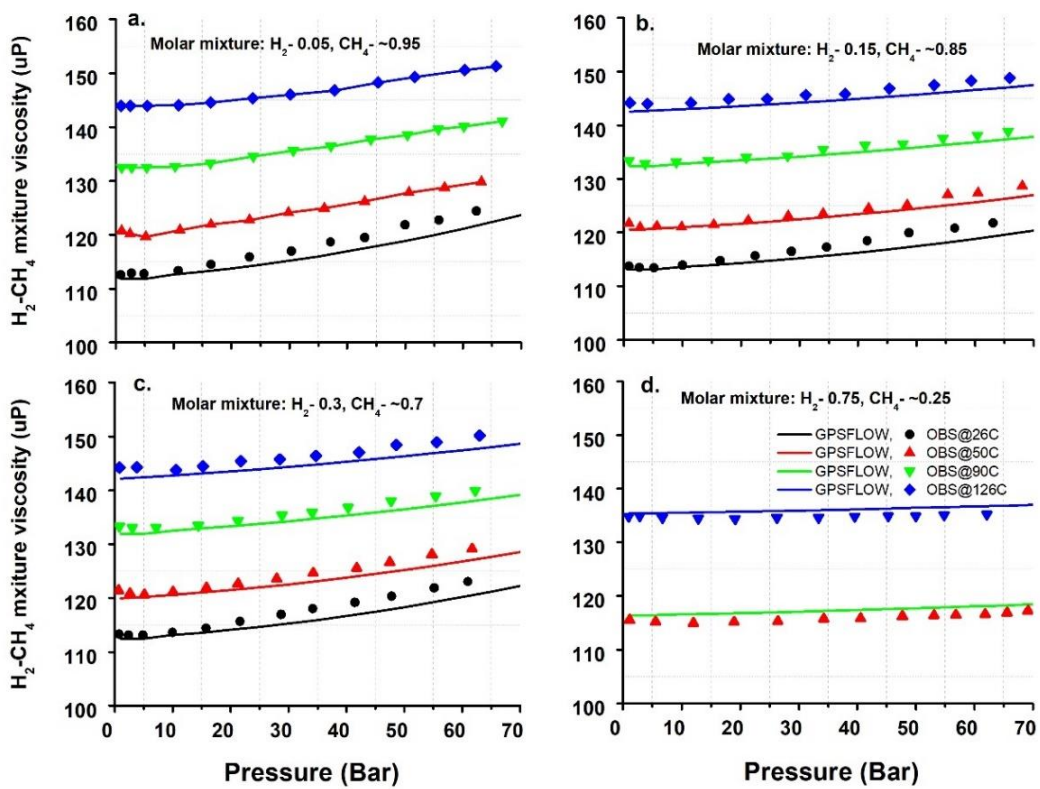


Figure 1 Comparisons of modelled and observed viscosity of H<sub>2</sub>-CH<sub>4</sub> gas mixtures from [63].

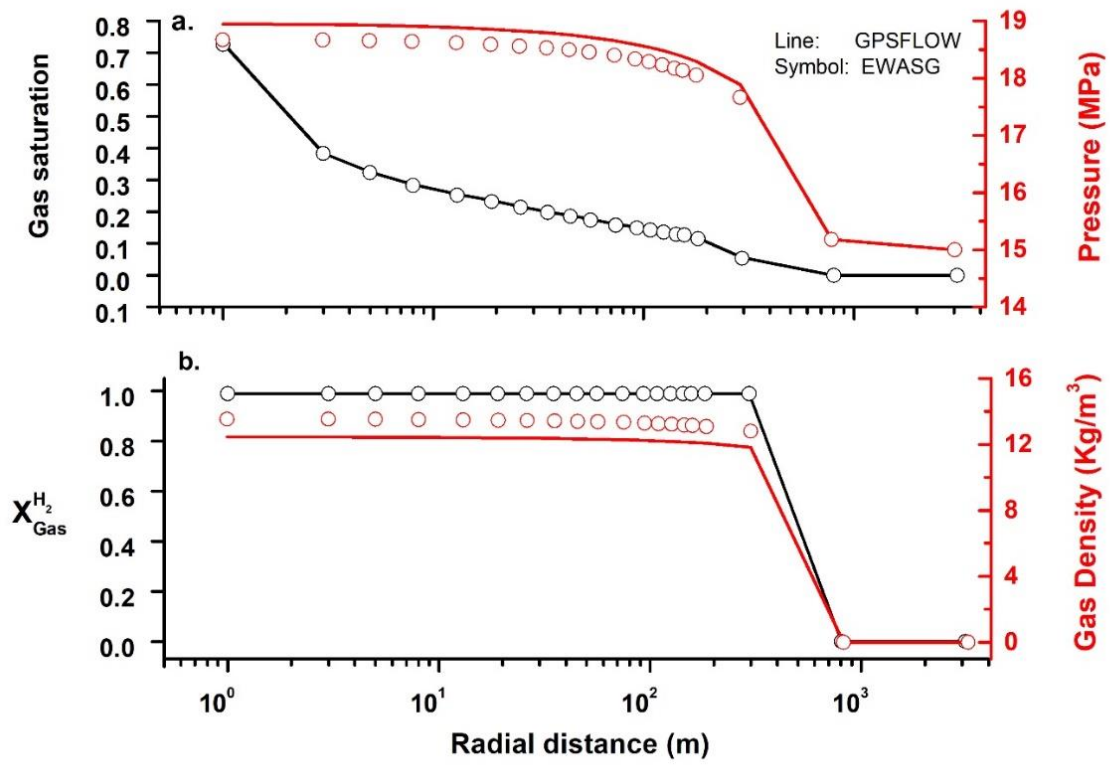


Figure 2. Comparison of the simulation result of H<sub>2</sub> injection into a 1D non-isothermal aquifer by GPSFLOW and TOUGH2/EWASG: (a) Gas saturation and reservoir pressure and (b) H<sub>2</sub> mass fraction ( $X_{gas}^{H_2}$ ) and H<sub>2</sub> gas density. The simulation time was 100 days.

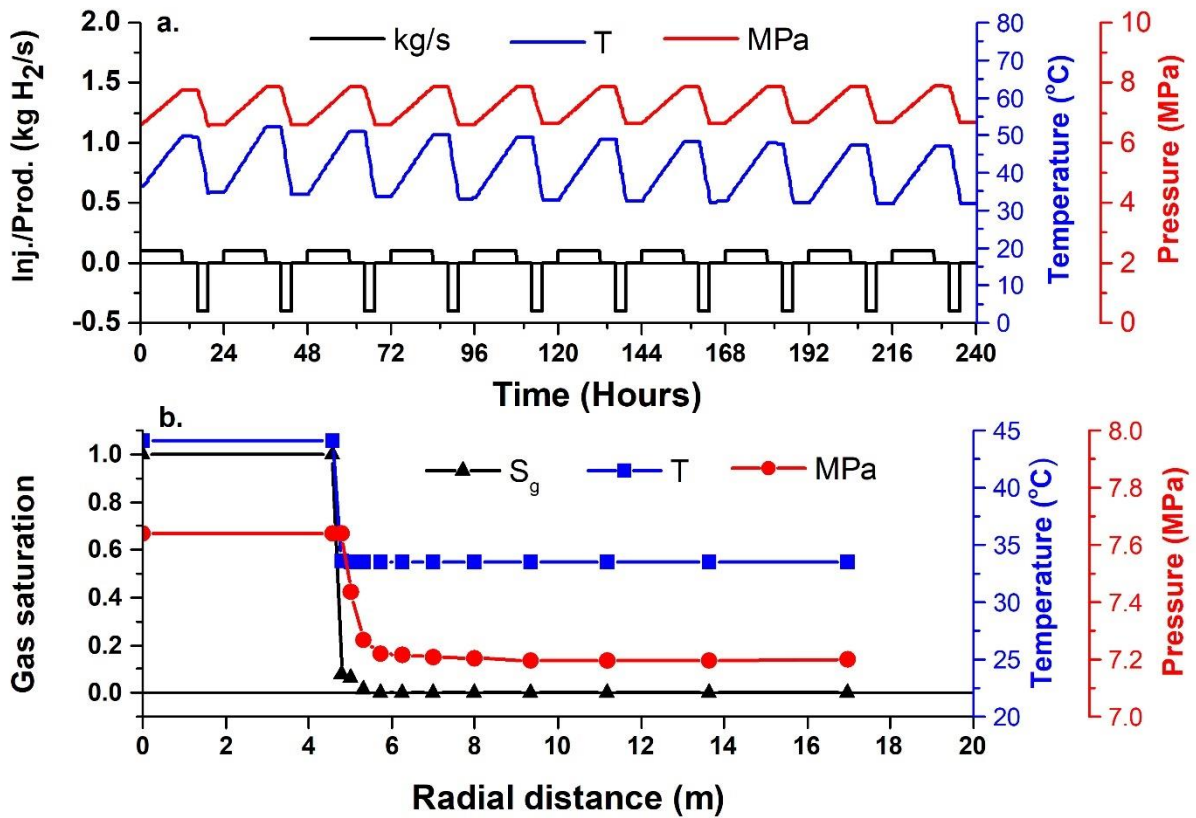


Figure 3. GPSFLOW for the modelling of daily H<sub>2</sub> storage cycle in a salt cavern: (a) H<sub>2</sub> injection and production cycle and its corresponding temperature and pressure within the cavern; (b) Gas saturation, temperature and pressure within the cavern and its surrounding rock after 10 daily cycles.

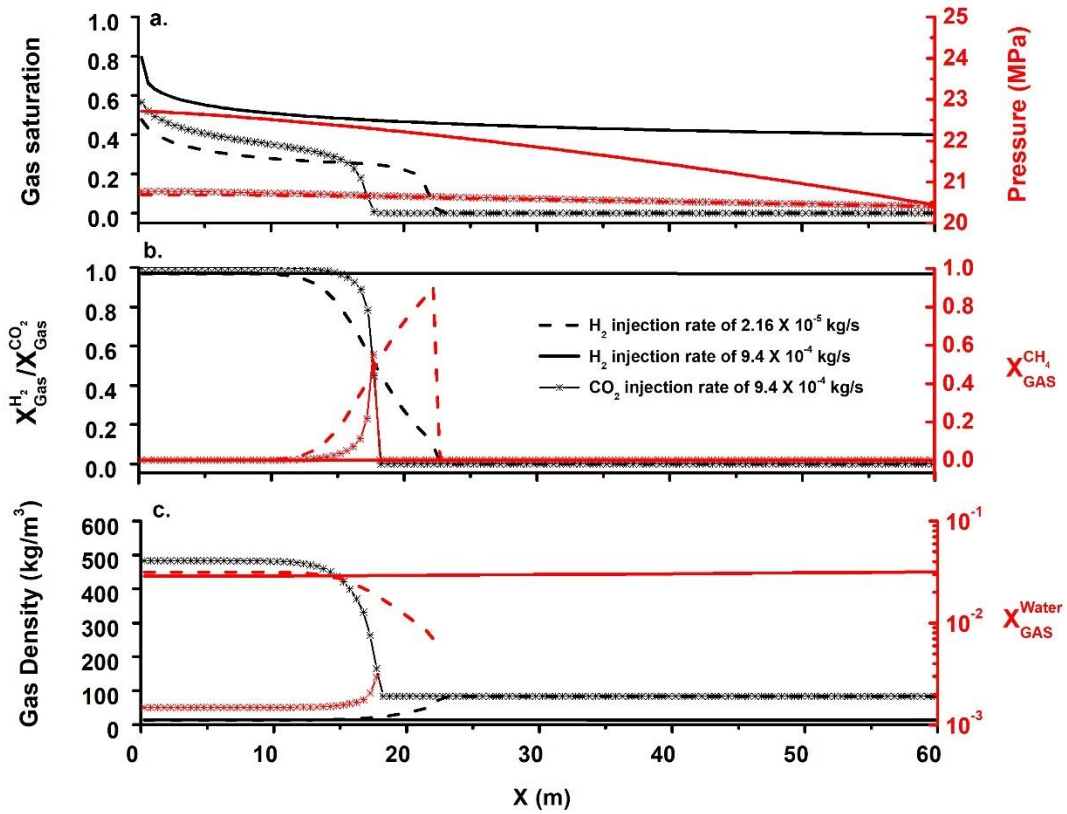


Figure 4. GPSFLOW for modelling H<sub>2</sub> and CO<sub>2</sub> single gas injection into a CH<sub>4</sub>-saturated aquifer experiment: (a) gas saturation and pressure along the distance; (b) mass fraction of H<sub>2</sub> and CO<sub>2</sub> in the gas phase; (c) gas density and water vapour mass fraction in the gas phase. The simulation time was 1 day.

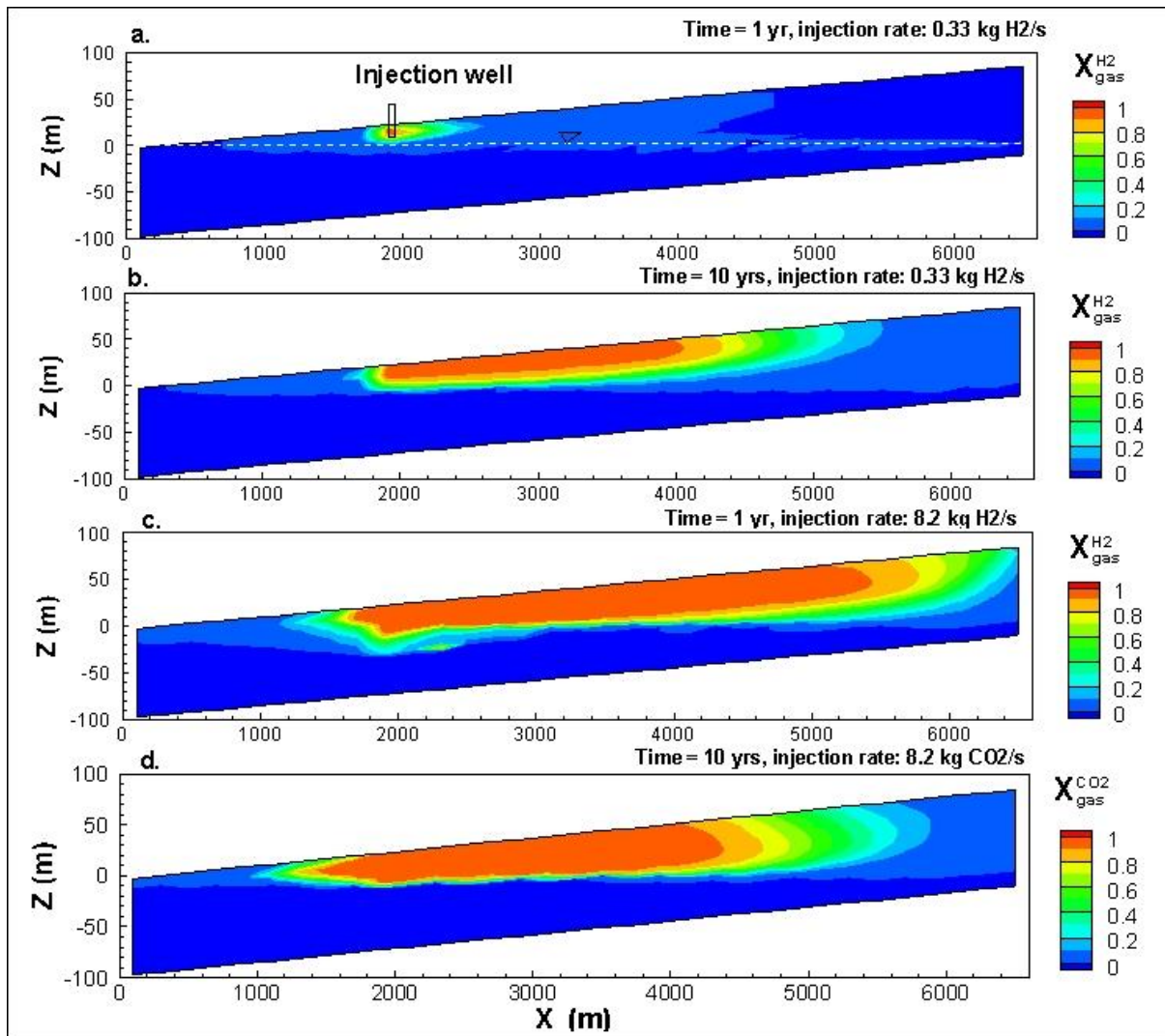


Figure 5. Mass fraction in the gas phase with no CH<sub>4</sub> production: a) & b) H<sub>2</sub> mass fraction with the injection rate of 0.33 kg H<sub>2</sub>/s after 1 and 10 years, respectively; c) H<sub>2</sub> mass fraction with the injection rate of 8.2 kg H<sub>2</sub>/s after 1 year; d) CO<sub>2</sub> mass fraction with the injection rate of 8.2 kg CO<sub>2</sub>/s after 10 years.

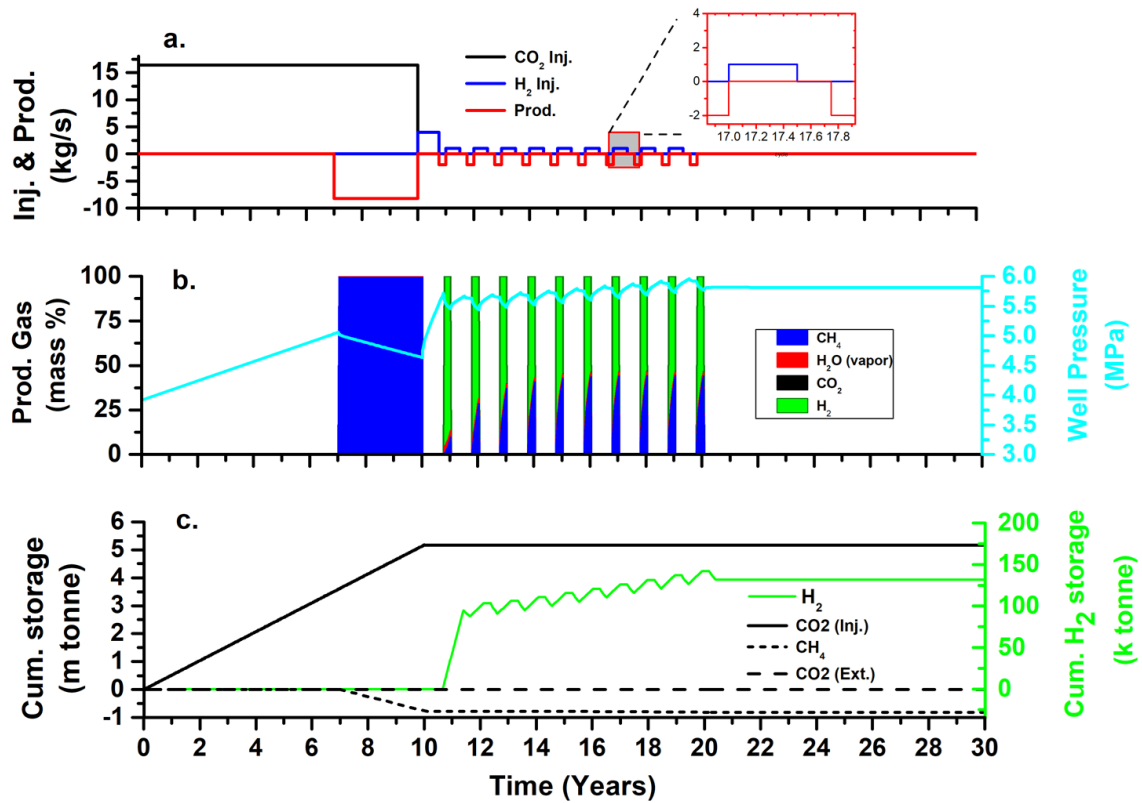


Figure 6. Simulation of CO<sub>2</sub> as cushion gas for H<sub>2</sub> storage in a depleted gas field: a) CO<sub>2</sub> injection, gas production, H<sub>2</sub> bubble development and H<sub>2</sub> injection/production cycle; 2) mass fraction of production gas mixture and pressure at the injection/production well; c) cumulative CO<sub>2</sub> injection and extraction, H<sub>2</sub> storage and CH<sub>4</sub> production.

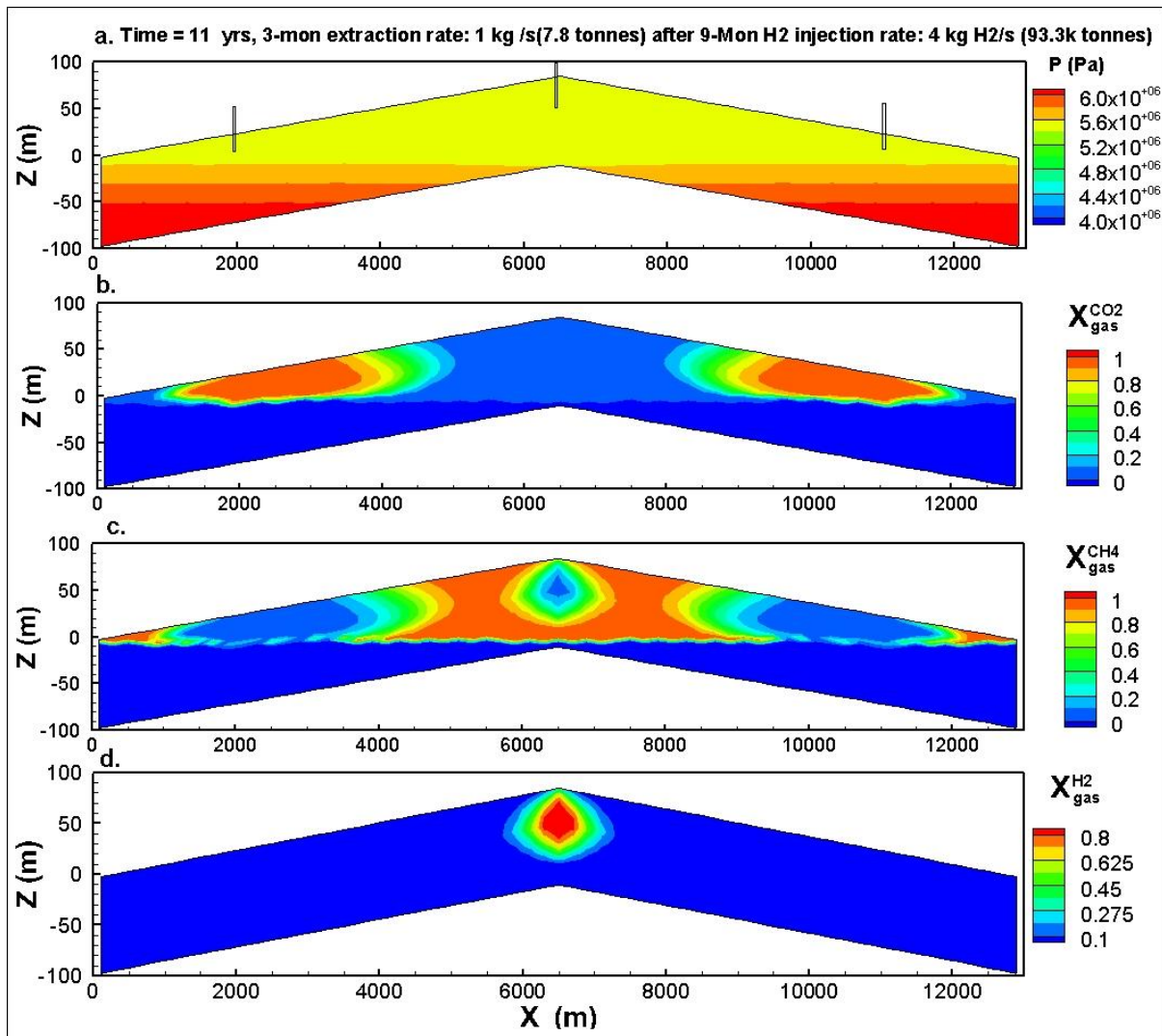


Figure 7. Pressure, mass fractions of CO<sub>2</sub>, CH<sub>4</sub> and H<sub>2</sub> in the gas phase after the H<sub>2</sub> bubble development and H<sub>2</sub> production at the end of Year 11.

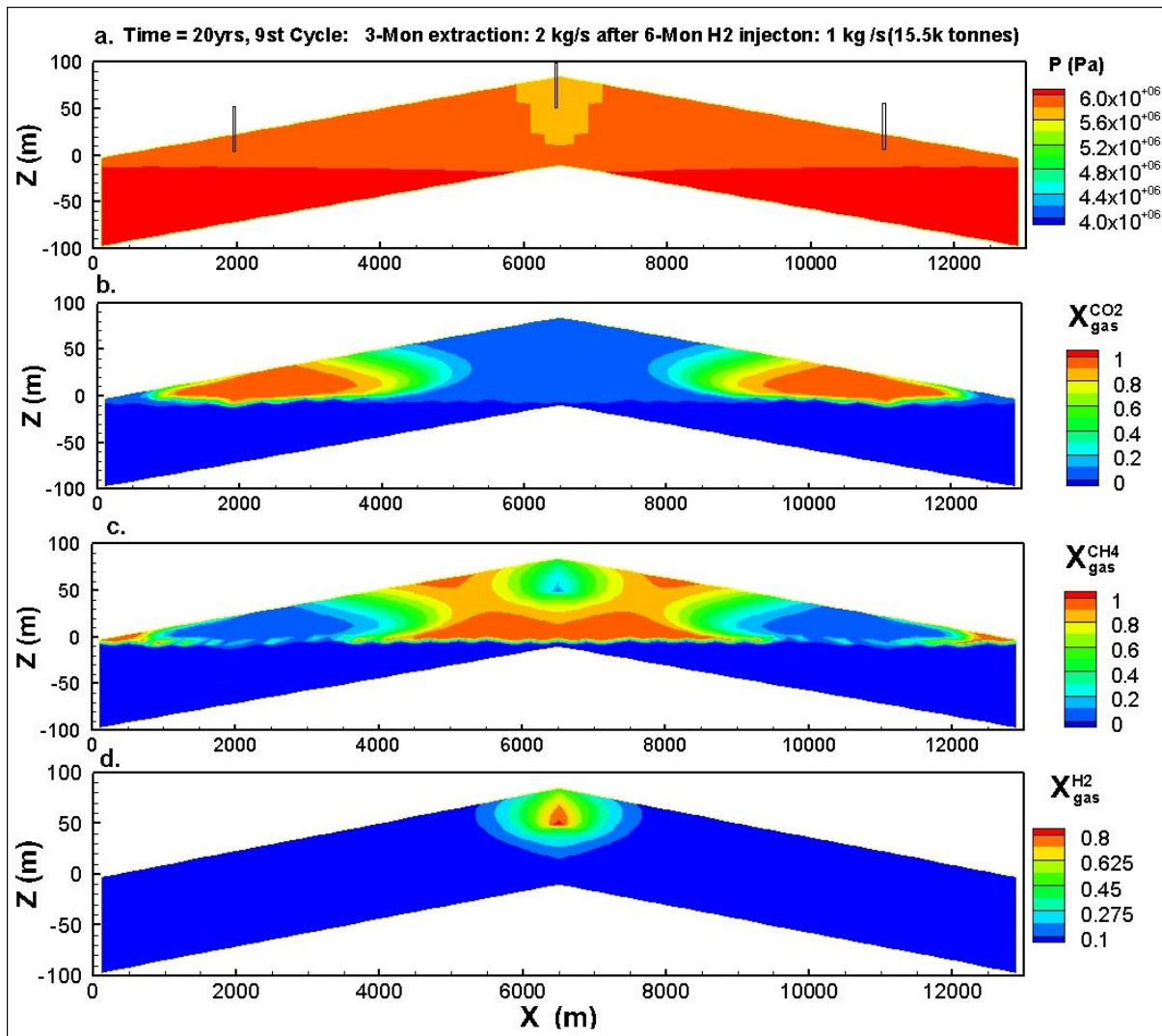


Figure 8. Pressure, mass fractions of CO<sub>2</sub>, CH<sub>4</sub> and H<sub>2</sub> in the gas phase after the 9<sup>th</sup> H<sub>2</sub> injection and production at the end of Year 20.

## Supplementary materials

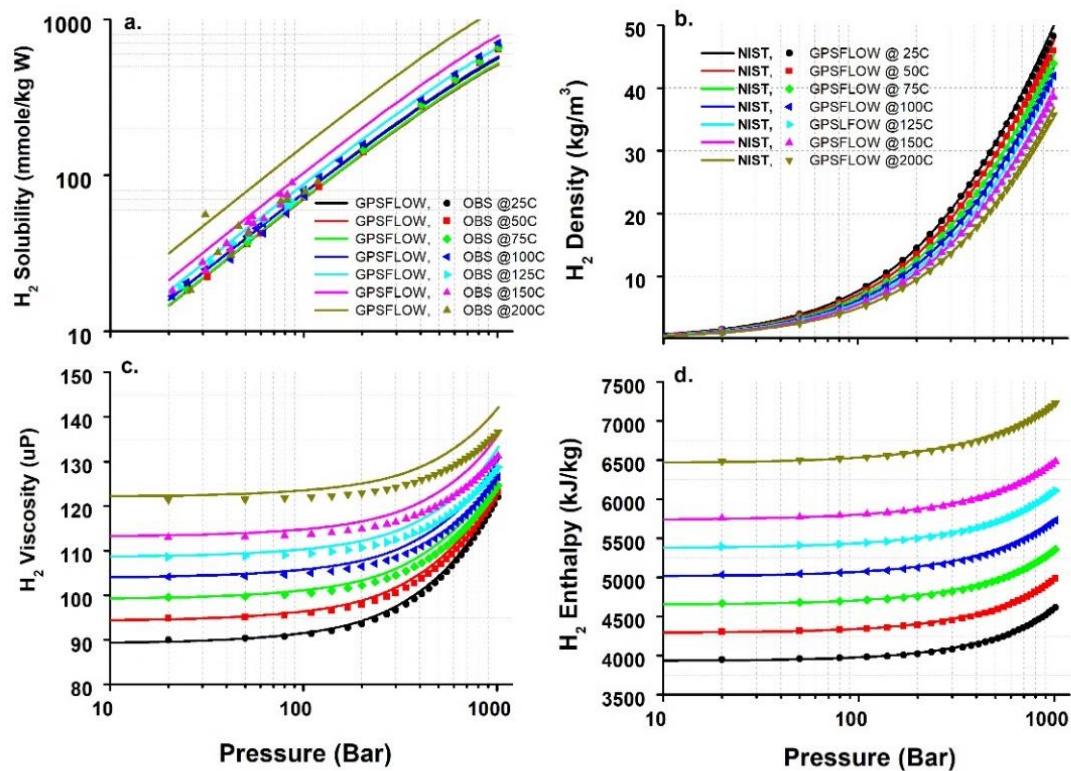


Figure S1. Comparisons of modelled results of pure H<sub>2</sub> gas against: a) laboratory-reported solubility in pure water [30, 37]; b) density obtained from the NIST database; c) viscosity obtained from the NIST database; d) enthalpy obtained from the NIST database.

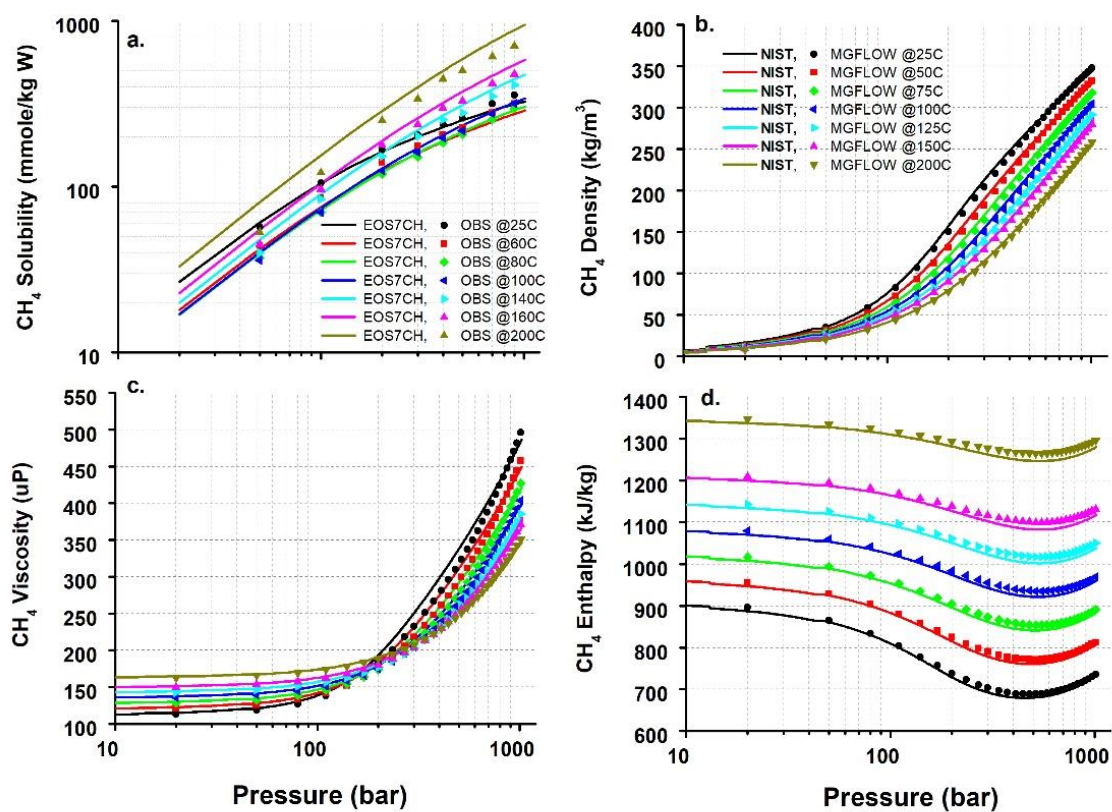


Figure S2. Comparisons of modelled results of pure CH<sub>4</sub> gas against: a) laboratory-reported solubility in pure water [41]; b) density obtained from the NIST database; c) viscosity obtained from the NIST database; d) enthalpy obtained from the NIST database.

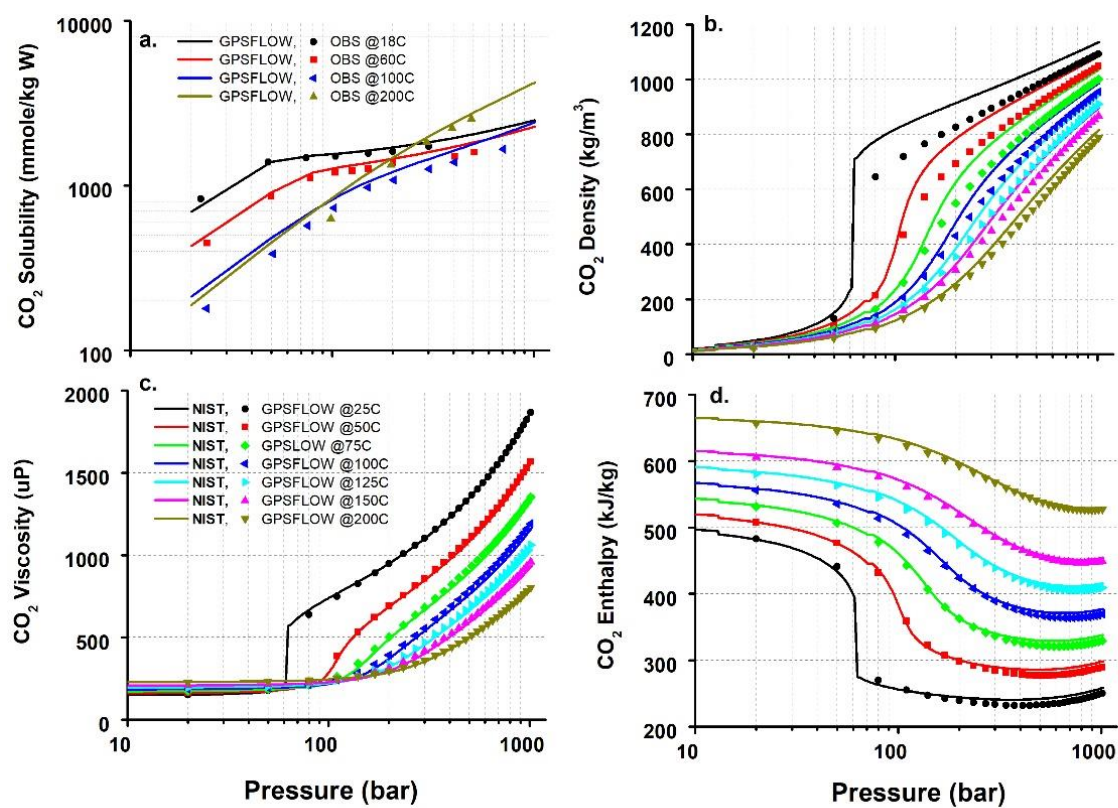


Figure S3. Comparisons of modelled results of pure CO<sub>2</sub> gas against: a) laboratory-reported solubility in pure water [39]; b) density obtained from the NIST database; c) viscosity obtained from the NIST database; d) enthalpy obtained from the NIST database.

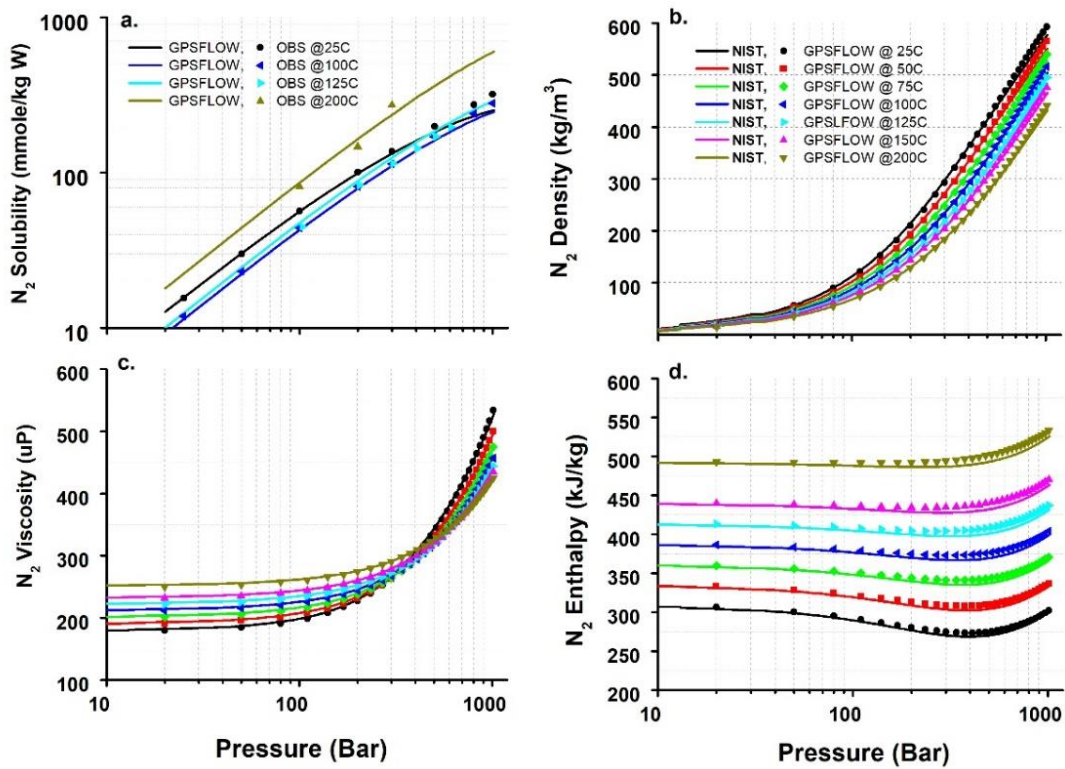


Figure S4. Comparisons of modelled results of pure N<sub>2</sub> gas against: a) laboratory-reported solubility in pure water [38, 40]; b) density obtained from the NIST database; c) viscosity obtained from the NIST database; d) enthalpy obtained from the NIST database.